A study of the accommodation of coherency strain by interfacial defects at a grain boundary in gold

Robert Charles Pond, Douglas L Medlin, Anna Serra

A study of the accommodation of coherency strain by interfacial defects at a grain boundary in gold

Journal:	*Philosophical Magazine & Philosophical Magazine Letters*
Manuscript ID:	TPHM-05-Dec-0577.R1
Journal Selection:	Philosophical Magazine
Date Submitted by the Author:	09-Mar-2006
Complete List of Authors:	Pond, Robert; The University of Liverpool, Engineering Medlin, Douglas; Sandia National Labs., Materials Physics Serra, Anna; Universitat Politecnica de Catalunya, Matematica Aplicada III
Keywords:	HRTEM, defect analysis, dislocations, grain boundary structure, molecular dynamic simulations, topological theory of defects
Keywords (user supplied):	

R.C. Pond[†], D.L. Medlin[††] and A. Serra[†††]

[†]Department of Engineering (Materials), University of Liverpool, Liverpool L69 3BX, United Kingdom.

[††] Sandia National Laboratories, Livermore, California, 94551, USA

[†††]Departament de Matemàtica Aplicada III, Universitat Politècnica de Catalunya, ETSE Camins, Jordi Girona 1-3, 08034 Barcelona, Spain.

ABSTRACT

The structure of a <110> 90° grain boundary in Au is investigated using high-resolution transmission electron microscopy (HRTEM) and atomistic simulation. It consists of coherent segments, exhibiting the extended 9R configuration as described by Medlin et al. (2001), with superimposed line-defects to accommodate the coherency strain. Two types of defects are observed, crystal dislocations and disconnections, where the latter exhibit step nature in addition to dislocation character. Both types of defect are identified by HRTEM in combination with circuit mapping, and their parameters are shown to be consistent with the topological theory of interfacial defects (Pond 1989). Moreover, the misfit-relieving function of observed defect arrays, their influence on interface orientation and the relative rotation of the adjacent crystals is elucidated. During observation, defect decomposition is observed in a manner which conserves Burgers vector and step height. One of the decomposition products is glissile, consistent with the 'glide/climb' rules for interfacial defects. This glissile motion is also found by atomistic simulation of the disconnection when an applied strain is imposed. The γ-surface for the interface is calculated and shows that no alternative boundary structure is stable, confirming, consistently with experimental observation, that defects separating different configurations are not feasible.

§ 1. INTRODUCTION

Transmission electron microscopy (TEM) has proved to be invaluable for the study of dislocations in crystalline materials [1,2]. The technique has enabled the characterisation of defects not only in the bulk of single crystals, but also those in interfaces, where they have important structural functions and dynamic roles [3]. The objective of the present article is to describe the accommodation of coherency strain in a grain boundary in Au, extending a recent preliminary account [4]. This observation is novel and interesting for two reasons; first, coherency strains are commonly encountered at inter-phase interfaces rather than grain boundaries [5]. Secondly, the coherency strains are accommodated in this case by interfacial line defects exhibiting step nature in addition to dislocation character. To emphasize the topological significance of combined dislocation/step character, Hirth [6] coined the term *disconnection* for a defect with line direction **ξ**, Burgers vector **b**, and step height h. In the present work we illustrate the characterisation of disconnections using TEM, how both **b** and h are conserved in defect reactions [7] and how accommodation of coherency strain by disconnections differs somewhat from that by dislocations [8].

§ 2. SPECIMEN PREPARATION

To produce the grain boundaries for this study, gold was deposited epitaxially onto [001] germanium. This procedure aligns {200} planes of Au parallel with {220} planes of Ge [9], thereby producing interlocking <110> oriented grains of Au in two crystallographic variants that are related to each other by a 90° rotation about the shared <110> axis. Prior to growth, the germanium substrate was cleaned successively in acetone, methanol, and ethanol, and then etched for several minutes in a 10% HF solution. Gold (99.99%) was evaporated onto the germanium substrate from a tungsten wire basket (~75Å/s; T = 250 °C) in a bell-jar deposition system (~10^{-7} Torr). After growth, the substrate was dissolved in a 50%HF:50%HNO_3 solution and the film was floated onto a gold TEM grid. The supported film was then mounted in an electron microscope heating stage and annealed under the microscope vacuum by gradually increasing the temperature to 680°C over a period of 1 hour.

Grain boundary structure was analysed at room temperature using a JEOL 4000EX high-resolution transmission electron microscope (HRTEM) (E = 400 keV, Scherzer resolution = 1.7Å). An example is illustrated in the HRTEM micrograph figure 1(a) which shows a grain boundary meandering between two crystals, designated λ and μ,

that are relatively rotated by 90° about the foil normal, $[\bar{1}01]_{\lambda\mu}$. In the enlargement of the planar segment, figure 1(b), coherent regions of the interface exhibit an extended 9R structure by emission into the λ crystal of partial dislocations trailing stacking-faults [10]. Superimposed on the coherent structure, four line-defects are seen end-on in the micrograph centred on the bright spots; the upper left defect is a crystal dislocation (**b**, 0) and the other three are disconnections (**b**, h). All of these defects contribute to the accommodation of the coherency strain and some were observed to decompose during observation.

§ 3. TOPOLOGICAL CHARACTER OF DEFECTS

3.1 *Admissible interfacial defects*

Line-defects that separate energetically degenerate regions of interface are referred to as admissible defects, and their topological characteristics are determined by the misorientation and symmetry of the adjacent crystals [7]. In the present application, two types of defects can accommodate misfit strain, namely crystal dislocations and disconnections. The former have Burgers vectors corresponding to translation vectors belonging to one of the adjacent crystals, $\mathbf{t}(\lambda)_i$ or $\mathbf{t}(\mu)_j$. Disconnections can be visualised as pairs of collinear crystal dislocations, one from each of the two crystals, as depicted schematically in figure 2, so their Burgers vectors correspond to combinations of translation vectors. In figure 2, the λ and μ crystals are bonded together on the left to form an interface; the gap between the crystals on the right hand side of the incompatible surface steps must be closed by a Volterra operation to form a degenerate interfacial structure, and this operation defines the Burgers vector of the defect created. Thus, the Burgers vectors of admissible dislocations and disconnections belong to the set

$$\mathbf{b}_{ij} = \mathbf{t}(\lambda)_i - \mathbf{t}(\mu)^*_j , \qquad (1)$$

where the asterisk implies that $\mathbf{t}(\mu)^*_j$ is expressed in the coordinate frame of the upper crystal (the coordinate transformation matrix, $\mathbf{P}_c$, for this is given in appendix A). One of the translation vectors in expression (1) is null for the crystal dislocation case. The

Burgers vectors defined by expression (1) can be displayed graphically in a dichromatic pattern [11], figure 3, where the λ crystal's lattice sites are white and the μ one's are black. The μ crystal in this figure has been uniaxially compressed parallel to $\left[1\bar{2}1\right]_{\mu}$ by 5.7% to become coherent with the λ. Using the FS/RH convention [12] for defects with ξ parallel to $\left[\bar{1}01\right]_{\lambda\mu}$, the Burgers vectors of disconnections correspond to 'black-to-white' vectors whereas those of crystal dislocations join sites of the same colour.

Disconnections exhibit finite 'overlap' step character, [13]; the surface step heights depicted in the schematic illustration of the formation of a disconnection, figure 2, are equal to $h(\lambda)_i = \mathbf{n} \bullet \mathbf{t}(\lambda)_i$ and $h(\mu)_j = \mathbf{n} \bullet \mathbf{t}(\mu)^*_j$, where **n** is the upward unit normal of the interface, and the step height, h, of the disconnection produced after bonding the surfaces together is the smaller of these two values. In the present case, h(λ) and h(μ) correspond to integral numbers of $\left(2\bar{4}2\right)_{\lambda}$ and $\left(\overline{111}\right)_{\mu}$ planes , so it is convenient to re-express $\mathbf{b}_{ij}$ as $\mathbf{b}_{\lambda/\mu}$ where λ and μ are the relevant integers. Using this notation, the topological character of the admissible defects of interest in this work are listed in Table 1; for crystal dislocations either λ or μ is zero, such as defect $\mathbf{b}_{1/0}$, whereas both λ and μ must be finite for disconnections, e.g. defects $\mathbf{b}_{-5/-2}$, $\mathbf{b}_{-8/-3}$, $\mathbf{b}_{-2/-1}$ and $\mathbf{b}_{3/1}$. We note that the $\mathbf{b}_{\lambda/\mu}$ notation is not unique since translation vectors parallel to the interface are present in both crystals, i.e. a multiplicity of defects with the same step character but different **b** potentially exist, as illustrated in figure 2 for two '-5/-2' disconnections. Nevertheless, in the present context, the notation is helpful for the specified defects since it conveys the nature of the λ and μ crystal steps.

.

3.2. *Defect decomposition*

Interfacial defects are liable to decompose if the free energy of the system thereby decreases. In principle, dissociation into partials bounding a different interface configuration can occur, but no evidence for this was found in the present study (see discussion of the γ-surface for the coherent structure below). Alternatively, defects can decompose into admissible reaction products provided the initial $\mathbf{b}_{\lambda/\mu}$, h(λ) and h(μ) are conserved. Frank's rule may be used to estimate the change of elastic energy, but atomistic calculations are needed to determine core energy contributions.

Decomposition at temperatures below about $T_m/2$ is improbable if long-range diffusion is required. Thus, for feasible reactions at modest temperatures, at least one of the products should be capable of conservative motion along the interface and have reasonable mobility under the prevailing driving force. The formal treatment for calculating the diffusional flux accompanying defect motion is set out in Appendix B following the treatment of [13] and it is shown that only disconnections with $\mathbf{b}_{\lambda/\mu}$ where $\lambda=3\mu$ move conservatively. Therefore, amongst the defects indicated in Table 1, only $\mathbf{b}_{3/1}$ can move conservatively. Importantly, this conservative motion occurs despite the defect having a component of Burgers vector parallel to **n**. This result is readily understood since, in the coherent state, the atomic density of a $(\bar{1}\bar{1}1)_\mu$ plane is three times that of a $(2\bar{4}\bar{2})_\lambda$ plane, so disconnection motion, causing material exchange from 3 planes of the λ grain to one plane of the μ, conserves atoms. Thus, two examples of feasible decompositions are

$$\mathbf{b}_{-5/-2} = \mathbf{b}_{-8/-3} + \mathbf{b}_{3/1} \qquad (2a)$$

and

$$\mathbf{b}_{1/0} = \mathbf{b}_{3/1} + \mathbf{b}_{-2/-1}. \qquad (2b)$$

These expressions show explicitly that surface step heights, as defined in figure 2, are conserved.

3.3. *Misfit accommodation*

In the present system the black crystal is imagined to be elastically compressed with respect to the white to form a coherent interface structure; subsequently, defects with edge components corresponding to 'extra half planes' in the white crystal are envisaged to plastically relieve this coherency strain. All the defects listed in Table 1 have this character, so, subject to their stability, are candidates for forming a misfit relieving array. Thus, for example, an array of $\mathbf{b}_{1/0}$ crystal dislocations with spacing

$$d = b_e/\varepsilon, \qquad (3)$$

where $\mathbf{b}_e$ is the edge component parallel to $[\bar{1}\bar{1}1]_\lambda / [\bar{1}2\bar{1}]_\mu$ and ε is the misfit strain, would relieve the misfit [12]. (To avoid introducing shears, an alternating array of

$1/2[\bar{1}10]_\lambda$ and $1/2[0\bar{1}\bar{1}]_\lambda$ dislocations would be necessary; amongst those listed in Table 1, the $\mathbf{b}_{1/0}$ defects are the only ones having a screw component.) The normal component, b_n, of these defects would not contribute to misfit relief but would cause the adjacent crystals to be relatively rotated by

$$\phi = b_n/d. \qquad (4)$$

Similarly, an array of disconnections could accommodate misfit, although the step character of these defects causes the average interface plane to deviate by an angle θ from the reference interface. To remove the misfit along this inclined interface plane, the disconnections must be appropriately spaced and, as outlined in Appendix C following the treatment of Pond et al. [8], the resulting value of θ is obtained from

$$-\varepsilon = \left(b_e \tan\theta + b_n \tan^2\theta\right)h^{-1}. \qquad (5)$$

In the present case the strain ε is equal to –0.057, corresponding to compression of the μ crystal with respect to the λ. Using expression (5), the angle θ can be calculated for an array of disconnections with known parameters, **b** and h, and hence the disconnection spacing along the coherent interface, equal to

$$d = h/\tan\theta, \qquad (6)$$

can be determined. Thus, the rigid-body tilt introduced by this array is given by [8]

$$\phi = 2\sin^{-1}\left[\left(b_n\cos\theta - b_e\sin\theta - \varepsilon h\cos\theta\right)\sin\theta/2h\right]. \qquad (7)$$

Of course, the expressions above strictly refer to infinitely long interfaces, but provide a useful framework for discussion in the present study. By comparing expression (3) with (6) and (4) with (7), it is clear that step character of disconnections is pertinent to misfit accommodation.

§ 4. Experimental Observations

4.1. *$b_{-5/-2}$ Disconnections*

The three defects to the lower right in figure 1(b) are $\mathbf{b}_{-5/-2}$ disconnections of the type depicted on the left of figure 2 and catalogued in Table 1; this is confirmed by circuit mapping [14, 4] as illustrated in figure 4. The circuit is divided into separate paths, $\mathbf{C}_\lambda$ and $\mathbf{C}_\mu$, in the two crystals. It is important that the two intersections of the circuit with the μ-9R interface be chosen at equivalent points as this ensures that these

segments (**EF** and **IA** in this example) cancel in the final vector sum. Furthermore, as discussed in §6, the λ circuit segment must extend beyond the 9R-λ region to avoid crossing the stacking-faults. $\mathbf{C}_\lambda$, (**ABCDE**), and $\mathbf{C}_\mu$, (**FGHI**), are summarised in Table 2. Note that both $\mathbf{C}_\lambda$ and $\mathbf{C}_\mu$ must possess components of $\pm\frac{1}{4}[\bar{1}01]$. Since the HRTEM image is sensitive only to the projected structure in this direction, the ambiguity in the sign cannot be resolved. For simplicity, we will take these components as oppositely signed and therefore cancelling out, giving a defect with pure edge content. It is conceivable, however, that these components could be of the same sign, in which case the defect would also have a screw component of $\pm\frac{1}{2}[\bar{1}01]$. The circuit can be mapped into the coherent dichromatic pattern either graphically or, as is done here, mathematically. Evaluating the closure failure of the circuit described in Table 2 with respect to the coherent reference frame, *i.e.* $\mathbf{b} = -(\mathbf{C}_\lambda + \mathbf{P}_c\mathbf{C}_\mu)$, gives the following result, expressed in the λ coordinate system:

$$\mathbf{b} = \tfrac{1}{36}\left[12\sqrt{2}-31,\quad -24\sqrt{2}+14,\quad 12\sqrt{2}-31\right] = [-0.390, -0.554, -0.390]. \qquad (8)$$

The measured dislocation content of the step is identical with that predicted by equation (1) and the observed step heights in the two crystals, h(λ) and h(μ), which are given by the perpendicular components of the two halves of the circuit, are $h(\lambda) = \mathbf{EA} \bullet n = -5a/2\sqrt{6}$, (i.e., five $(2\bar{4}2)_\lambda$ planes), and $h(\mu) = \mathbf{FI} \bullet n = -2a/\sqrt{3}$ (two $\{111\}_\mu$ planes). Reference to the left-hand disconnection in figure 2 then suggests $\mathbf{t}(\mu)$ is $\frac{1}{2}[112]_\mu$ and $\mathbf{t}(\lambda)$ is $\frac{1}{2}[\bar{2}1\bar{1}]_\lambda$ which gives a Burgers vector in agreement with that deduced from the circuit map. The small component b_n (see Table 1) arises from the mismatch in step heights, $a(2/\sqrt{3} - 5/2\sqrt{6})$, where a represents the lattice parameter. The component b_e is larger and in λ coordinates possesses a magnitude equal to $4a/3\sqrt{3}$. Re-expressed in the μ coordinate frame, the magnitude of this component is $2a/\sqrt{6}$, which can be interpreted as a deficit of four $(2\bar{4}2)$ planes in the μ crystal. According to expressions 5, 6 and 7, the theoretical values of θ, d and ϕ are –4.38°, 6.49nm and +0.58° respectively which are in reasonable agreement with the observed values of -4.3° ± 0.25°, 6.75nm ± 0.3nm and 0.97° ± 0.08°.

4.2. *Decomposition of $b_{-5/-2}$ Disconnections*

Some of the $\boldsymbol{b}_{-5/-2}$ disconnections were observed to be decomposed into $\mathbf{b}_{-8/-3}$ and $\mathbf{b}_{3/1}$ disconnections, as in expression 2(a), and an example is shown in figure 5. Relevant translation vectors and step heights for the decomposition products are illustrated in the dichromatic pattern, figure 6. Circuit mapping was used to confirm the (**b**, h) character of the $\mathbf{b}_{-8/-3}$ and $\mathbf{b}_{3/1}$ defects (see Table 2). The $\mathbf{b}_{3/1}$ disconnection has evidently moved along the interface and come to rest equidistantly from the neighbouring disconnections, as expected since it is repulsed by these. Its glissile nature was also confirmed using molecular dynamic simulation, as discussed later.

4.3. *$b_{1/0}$ Dislocations*

The defect shown in figure 7 is a $\mathbf{b}_{1/0}$ crystal dislocation as confirmed by circuit mapping, Table 2. Notice that the μ crystal surface is not stepped at this defect; i.e. the circuit segment $\mathbf{C}_\mu = 3\left[\bar{1}2\bar{1}\right]_\mu$ is parallel to the notional μ crystal surface, corresponding to $\mathbf{t}(\mu)_j$ being the null vector in equation (1).

4.4. *Decomposition of $b_{1/0}$ Dislocations*

Some of the $\mathbf{b}_{1/0}$ dislocations were observed to be decomposed according to the reaction in expression 2(b), as illustrated in figure 8. Circuit mapping was used to confirm the (**b**, h) character of the $\mathbf{b}_{-2/-1}$and $\mathbf{b}_{3/1}$ defects, Table 2. Again, the glissile $\mathbf{b}_{3/1}$ disconnection has moved along the interface, repelled by the $\mathbf{b}_{-2/-1}$ disconnection. The relevant translation vectors and step heights for this decomposition are depicted in the dichromatic patterns, figure 9.

§ 5. ATOMISTIC SIMULATIONS

5.1. *Mobility of $\boldsymbol{b}_{3/1}$ disconnections*

The motion of $\mathbf{b}_{3/1}$ disconnections was investigated by atomistic simulation using an EAM type many-body potential for gold [10] fitted with the values of experimental elastic constants, vacancy formation energy and stacking fault energy. The simulated systems were bicrystals containing up to ~35000 mobile atoms. Fixed boundary conditions were used in the direction perpendicular to the interface; the distance from the interface to each fixed boundary was 22 lattice parameters ensuring a negligible

interaction of the interface with the boundaries. Periodic boundary conditions were used in the plane containing the interface. The boundary conditions are straightforward for the $[\bar{1}01]$ direction which is common to both crystals but the periodicity along $[111]_\lambda/[1\bar{2}1]_\mu$ has to be imposed by slightly modifying the total length of one of the crystals along that direction, and the μ crystal was uniaxially compressed by 5.7% along $[1\bar{2}1]_\mu$. Stable atomic structures were relaxed using a combination of conjugate gradients and molecular dynamics; the 9R structure arises spontaneously during this procedure.

The mobility of $\mathbf{b}_{3/1}$ disconnections was studied using a technique implemented by Osetsky and Bacon [15] for the simulation of a periodic array of crystal dislocations with periodic boundary conditions not only along the dislocation line but along the Burgers vector direction. The method can simulate long-distance motion of a dislocation under a variety of loading and temperature conditions. The method has been extended to the simulation of glissile disconnections in twin boundaries by Serra and Bacon [16]. The $\mathbf{b}_{3/1}$ disconnection was introduced in the coherent interface by selecting the two largest translation vectors in the bicrystal, $\mathbf{t}(\lambda)_i$ and $\mathbf{t}(\mu)_j$, whose difference is the Burgers vector $\mathbf{b}_{3/1}$ according to equation (1). Then, the two crystals are strained to bring $\mathbf{t}(\lambda)_i$ and $\mathbf{t}(\mu)_j$ into coincidence. In this way the strain field associated with the dislocation is introduced into the unrelaxed system. The vector used to generate periodicity along the horizontal direction, i.e. the translation vector $\mathbf{t}^*$ of the model supercell, can be chosen to be $\mathbf{t}^* = 1/2(\mathbf{t}(\lambda)_i + \mathbf{t}(\mu)_j)$. After the straining process, both crystals, λ and μ, have a lattice translation parallel to $\mathbf{t}^*$ and therefore periodic boundary conditions can be applied. Applying a shear strain of $2.5\text{x}10^{-4}$ to the bicrystal causes the $\mathbf{b}_{3/1}$ disconnection to move rapidly, confirming its glissile nature. When it leaves the simulation box at one side it appears at the opposite side moving the interface up/down according to sense of motion and step height. An instantaneous image of the defect's motion is shown in figure 10; its core is slightly left of the centre and the coherent interface plane is one $(111)_\mu$ plane higher to the right of the core than to the left. The shading of the atoms depicts the local hydrostatic pressure, which emphasizes the interface location and the extended structure of the 9R region with partial dislocation dipoles separated by stacking-faults. .

5.1. *γ-Surface*

Another point resolved by atomistic simulation relates to the experimental observation that no defects were found that separate regions of interface with different structures. This implies that only one interfacial structure is feasible, and this was tested by calculating the γ-surface for the system. The detailed structure of the coherent interface, as seen in figure 10, is identical to that simulated by Medlin et al. [10]. The γ-surface was calculated by displacing the λ crystal parallel to the μ-9R interface and allowing the system to relax only in the direction perpendicular to the interface and a contour plot is shown in figure 11. The 'cell of non identical displacements' is indicated; this centred rectangular cell has edges $\frac{1}{2}\left[\bar{1}01\right]_\lambda$ and $\frac{2}{3}\left[\overline{111}\right]_\lambda$. The energy values shown are obtained after subtraction of the strain energy of the compressed μ crystal from the total energy, thereby giving an estimate of the interfacial energy. It is clear from this plot that the observed structure, corresponding to the point at the origin of the cell, is the only stable structure, hence supporting the notion that no imperfect line defects are anticipated in this interface.

§ 6. Discussion and conclusions

Sutton and Balluffi [3], in their comprehensive summary of our current understanding of interfaces, classified grain boundaries into three categories: singular, vicinal and general. Singular interfaces have energies that are a minimum with respect to at least one of the macroscopic degrees of freedom, and superimposing arrays of line-defects accommodates angular deviations from these at vicinal boundaries. Most of the singular structures identified so far are periodic in the 2-D parallel to the interface, although there is accumulating evidence that configurations with 1-D periodicity arise (for example, see [17]). The boundary studied here illustrates another type of vicinal interface. Here one dimension, along the $\left[\bar{1}01\right]$ axis, is naturally periodic, but, perpendicular to this, periodicity can only be sustained by coherency strains in the adjacent crystals. Moreover, in a manner more typical of interphase or epitaxial interfaces, the coherency strains are accommodated by an array of line-defects.

The interface studied here exhibits an extended structure with partial dislocations emitted into the λ crystal on every third $(111)_\lambda$ plane, so it is important to comment on the possible role of this configuration in accommodating misfit. When regarded as an array, the partial dislocations located at the μ-9R interface act primarily as a low-angle tilt boundary, rotating the $(111)_\lambda$ planes by 6.7° [10]. This rotation, clearly seen in figures 4 and 5 for example, effectively increases the interplanar spacing of the $(111)_\lambda$ planes at the interface by the factor 1/cos6.7°, thereby reducing the misfit from 5.72% to 5.07% in the immediate vicinity of the interface. Of course, the array of partials at the 9R-λ interface introduces the opposite rotation, re-establishing the full 5.72% misfit. Thus, from a topological viewpoint, we may suppress this local relaxation when characterising interfacial defects able to accommodate the total misfit. Hence, it is permissible to construct dichromatic patterns where the μ crystal is uniformly compressed by 5.72%, as in figures 3, 6 and 9. Similarly, circuits constructed on HRTEM micrographs may be mapped into these dichromatic patterns, provided they do not intersect any stacking-faults, as in figures 4, 5, 7 and 8. Subject to this consideration, the disconnections and dislocations investigated in this work and the experimentally determined parameters are in precise agreement with the predictions of the topological theory of interfacial defects [7].

Although the disconnections act similarly to dislocation arrays in accommodating misfit strains, their step character needs to be taken into account. The steps cause the overall interface plane, or habit, to deviate by an angle θ from the coherent $(1\bar{2}1)_\lambda/(\overline{111})_\mu$ plane and the disconnection spacing, d, must be adjusted so that the misfit parallel to the habit plane is removed. Thus, the boundary inclination and mode of strain accommodation are closely coupled. Excellent agreement was found between the predicted and measured values of θ and d. In general, a rigid-body rotation, ϕ, between the adjacent crystals arises because of the component of effective **b** normal to the habit plane (i.e. including the contributions from the disconnections and the elastic coherency strain). A discrepancy of ~ 0.4° was found between predicted and observed values of ϕ; it is presumed that this arose due to the interference from rigid-body tilts associated with other segments of the same and other nearby interfaces.

The observed $\mathbf{b}_{-5/-2}$ disconnections appear to be favourable in their role of misfit accommodation. The smallest crystal lattice dislocations possessing Burgers vectors aligned entirely parallel with the interface ($[\bar{1}\,\bar{1}\,\bar{1}]_\lambda$ or $\frac{1}{2}[\bar{1}\,2\,\bar{1}]_\mu$) would have very large magnitudes (1.73a and 1.22a, respectively) and for this reason are likely to be unstable. In comparison, $|\mathbf{b}_{-5/-2}| = 0.781a$ is similar to that of a $\frac{1}{2}[\bar{1}\,\bar{1}\,0]_\lambda$ crystal lattice dislocation, 0.707a. Yet, because the perpendicular component of the disconnections is small (0.13a), these defects are able to accommodate the misfit efficiently. The core structures of the $\mathbf{b}_{-5/-2}$ disconnections, and other observed defects, could also be investigated using HRTEM; a programme of atomic simulation to determine possible core structures is currently in progress and image simulations based on these calculations will be compared with experimental micrographs.

The observed decomposition of $\mathbf{b}_{-5/-2}$ disconnections and $\mathbf{b}_{1/0}$ crystal dislocations in a manner consistent with equation 2 is to be expected according to Frank's rule [12]; the reduction in elastic energy is 37.4% and 32% in the two cases respectively. However, some defects, such as $\mathbf{b}_{-8/-3}$ disconnections, exhibit large step heights so their core energies may be significant; atomistic simulation of these defects is necessary to provide further information on this point.

Another interesting observation is the sessile nature of all the defects studied except for $\mathbf{b}_{3/1}$ disconnections, again consistent with the theoretical expectation described in Appendix B. This disconnection is glissile despite having a component of its Burgers vector normal to the coherent plane. At coherent interfaces where one or both of the crystals is elastically compressed/extended in the near-field region of the boundary, the densities of the two crystals differ. Thus, the 'glide/climb' rules for defects in interfaces are not the same as for their counterparts in single crystals. Disconnections are glissile as long as their motion leads to the transfer of atoms from one crystal to the other on a one-to-one basis; this process does not conserve volume where the crystals have different densities. The mobility of $\mathbf{b}_{3/1}$ disconnections is presumably limited by the extent of shuffling that must accompany motion [18]; in the present case, only one in every six atoms would be sheared into the correct site, the others having to shuffle distances up to $\sim \frac{a}{\sqrt{3}}$.

Atomistic simulation is an invaluable complement to TEM observations. In the present work, the glissile motion of $\mathbf{b}_{3/1}$ disconnections was found, as described in

section 5. Also, the absence of defects separating different interfacial structures in our TEM study has been explained by calculating the γ-surface, which shows that the observed interface configuration is the only stable structure. In future work, the authors will address the core structures of disconnections and dislocations in this interface and study further the mobility of $\mathbf{b}_{3/1}$ disconnections.

ACKNOWLEDGEMENTS

The authors are grateful to Drs. J.A. Brown, Y. Mishin and A. Barachev for valuable discussions. DLM was supported at Sandia National Laboratories by the U.S. Department of Energy, Office of Basic Energy Sciences, under Contract #DE-AC04-94AL85000. AS was supported by the Spanish MCYT [(BFM2003-08211-C03-03); the computing was carried out in CESCA (www.CESCA.es)

§. Appendix A

The matrix $\mathbf{P}_c$ re-expresses vectors of the black crystal in the coordinate frame of the white, i.e. $\mathbf{t}(\mu)^*_j = \mathbf{P}_c\ \mathbf{t}(\mu)_j$; the full derivation has been presented elsewhere [4] so only the final matrix is quoted here. The matrix represents both the compression of the black crystal and the rotation of its coordinate frame by 90° about the common $[\bar{1}01]$ direction,

$$\mathbf{P}_c = \frac{1}{18}\begin{pmatrix} (13-3\sqrt{2}) & (-8-3\sqrt{2}) & (-5-3\sqrt{2}) \\ (4+6\sqrt{2}) & (-8+6\sqrt{2}) & (4+6\sqrt{2}) \\ (-5-3\sqrt{2}) & (-8-3\sqrt{2}) & (13-3\sqrt{2}) \end{pmatrix} \quad \text{(A 1)}$$

§. Appendix B

The diffusional flux accompanying the motion of a disconnection along an interface was obtained by Hirth and Pond [13]; the line direction of the disconnection is x, and the interface plane is x,y. The number of atoms per unit volume in the natural crystals is X. When the two crystals are strained into coherency, their densities change. The misfit strain, ε, can be partitioned between the crystals in any chosen

manner, but here, for simplicity, the upper is unchanged and the lower crystal is compressed so its density increases to $(1+\varepsilon)^{-1}X$. For formal purposes, the step and dislocation portions of a disconnection can be treated separately, as illustrated schematically in figure B 1. Motion of the step portion causes *transfer* of material from one crystal to the other, and the magnitude of the flux depends on h and the difference between the densities of the two phases, $\Delta X = \varepsilon\ (1+\varepsilon)^{-1}X$. Motion of the dislocation portion alone would not involve transfer of material, and the magnitude of the flux is determined by b_n and the density of one of the crystals, the upper in the case illustrated. These two contributions to δN, the number of atoms diffusing to (positive values) or away from (negative values) the disconnection, are depicted schematically in figure B 1. When a unit length of disconnection moves by the distance δy, the incremental flux, δN, is given by

$$\delta N = (h\ \Delta X + b_n X\ )\delta y. \qquad \text{(B 1)}$$

This expression emphasizes the distinction between the glide/climb behaviour of crystal dislocations and disconnections along interfaces; in the former case h = 0, so glide occurs if b_n is zero. On the other hand, disconnections exhibit finite h and hence move conservatively only when the two terms in the bracket balance.

In the present case, $b_n = \lambda d_\lambda - \mu d_\mu$, where d_λ and d_μ are the interplanar spacing of the $(2\bar{4}2)_\lambda$ and $(\overline{111})_\mu$ planes respectively. Moreover, taking the case illustrated above, $h = \mu d_\mu$, so equation (A 1) can be re-expressed as

$$\delta N = X\{\mu d_\mu\ \varepsilon\ (1+\varepsilon)^{-1} + [\lambda d_\lambda - \mu d_\mu]\ \}\delta y. \qquad \text{(B 2)}$$

Furthermore, $\varepsilon = \left(\frac{4}{3\sqrt{2}} - 1\right)$, so $\varepsilon\ (1+\varepsilon)^{-1} = \left(1 - \frac{3\sqrt{2}}{4}\right)$, $d_\lambda = \frac{a}{\sqrt{24}}$ and $d_\mu = \frac{a}{\sqrt{3}}$,

where a is the natural lattice parameter. On substituting these values into (B 2), one obtains

$$\delta N = \frac{aX}{\sqrt{24}}[\lambda - 3\mu]\delta y \,. \qquad \text{(B 3)}$$

Thus, only disconnections for which $\lambda = 3\mu$ will move conservatively.

§. Appendix C

The macroscopic interface, or habit plane, is inclined at the angle θ to the plane of the coherent interface, as shown in figure C 1. The elastic coherency strain is represented by a 'coherency dislocation' array, with Burgers vector content per unit length equal to the misfit strain, ε. In figure C 1, this defect content is shown as a single dislocation symbol, $\mathbf{b}_c$, where $|\mathbf{b}_c| = d\,\varepsilon$, located half way between the evenly spaced disconnections. This elastic coherency strain is accommodated plastically by the disconnection array; for each disconnection, its step, of height h, is taken to be perpendicular to the coherent interface and its **b** (see Table 1) is assumed to be located midway up the step. To accommodate the coherency strain, the spacing of the disconnections must be adjusted until the total dislocation content parallel to the habit plane is zero, i.e. $\boldsymbol{b}'_{cx} = -\boldsymbol{b}'_{x}$. This condition enables θ to be found using expression (5), and hence the disconnection spacing, d, by equation (6). Although a short-range strain-field will persist, the coherency strain at longer range will be annulled. Residual Burgers vector components perpendicular to the habit plane, $\boldsymbol{b}'_{cz}$ and $\boldsymbol{b}'_{z}$, constitute a tilt wall with short-range strain-field, thereby producing the rigid-body rotation, ϕ, defined by equation (7).

REFERENCES

[1] Hirsch, P.B., Howie, A., Whelan, M.J., Nicholson, R.B. and Pashley, D.W., 1965, *Electron Microscopy of Thin Crystals* (Butterworths: London).

[2] Williams, D.B. and Carter,C.B, 1996, *Transmission Electron Microscopy* (Springer: New York).

[3] Sutton, A.P. and Balluffi, R.W., 1995, *Interfaces in Crystalline Materials* (Clarendon Press: Oxford).

[4] Medlin, D.L., Cohen, D. and Pond, R.C., 2003, *Phil. Mag. Letters,* **83,** 223.

[5] Howe, J.M., 1997, *Interfaces in Materials* (Wiley: USA).

[6] Hirth, J.P., 1994, *J. Phys. Chem. Solids* **55**, 985.

[7] Pond, R.C., 1989, *Dislocations in Solids*, ed. F.R.N. Nabarro (Elsevier Science Publishers) **8** Chapter 38, 1-66.

[8] Pond, R.C., Celotto S. and Hirth J.P., 2003, *Acta materialia*, **51**, 5385.

[9] Pénisson, J. -M., Lançon, F., and Dahmen, U., 1999, *Materials Science Forum*, **294-296**, 27.

[10] Medlin, D.L., Foiles, S.M., and Cohen, D., 2001, *Acta materialia*, **49**, 3689.

[11] Pond, R.C. and Vlachavas, D.S., 1983, *Proc. Roy. Soc. London*, A **386**, 95.

[12] Hirth, J.P. and Lothe, J., 1968, *Theory of Dislocations* (McGraw-Hill: New York).

[13] Hirth, J.P. and Pond, R.C., 1996, *Acta materialia*, **44**, 4749.

[14] Pond, R.C. and Hirth, J.P., 1994, *Solid State Physics*, **47**, 287.

[15] Osetsky, Yu.N. and Bacon, D.J., 2003, *Modelling Simulation in Materials Science*, **11**, 427.

[16] Serra, A. and Bacon, D.J., 2004, *Z. Metall.*, **95**, 4.

[17] Sarrazit, F., Pond, R.C. and Kiselev, N.A., 1998, Phil. Mag. Letts., **77**, 191.

[18] Crocker, AG ,1962, *Phil. Mag.* **7**, 1901.

FIGURE CAPTIONS

Figure 1. (a) Bright field TEM image showing the meandering morphology of the 90° <110> boundaries in the Au film. (b) Higher magnification image of the indicated

region from (a) showing a segment of coherent boundary with three superimposed disconnections and one crystal dislocation.

Figure 2. Schematic formation of $\mathbf{b}_{-5/-2}$ disconnections; the translation vectors defining the incompatible surface steps on the adjacent crystals are indicated.

Figure 3. Dichromatic pattern for the coherent crystals, with $\mathbf{t}(\lambda)_i$ and $\mathbf{t}(\mu)_j$ for the disconnection $\mathbf{b}_{-5/-2}$ on the left of figure 2 indicated.

Figure 4. HRTEM image showing a closed circuit encircling a $\mathbf{b}_{-5/-2}$ disconnection.

Figure 5. HRTEM image showing a closed circuit encircling a $\mathbf{b}_{-5/-2}$ disconnection after decomposition into $\mathbf{b}_{-8/-3}$ and $\mathbf{b}_{3/1}$ defects.

Figure 6. Dichromatic pattern showing the relevant translation vectors and step heights for $\mathbf{b}_{-8/-3}$ and $\mathbf{b}_{3/1}$ disconnections.

Figure 7. HRTEM image showing a closed circuit encircling a $\mathbf{b}_{1/0}$ dislocation.

Figure 8. HRTEM image showing a closed circuit encircling a $\mathbf{b}_{1/0}$ dislocation after decomposition into $\mathbf{b}_{3/1}$ and $\mathbf{b}_{-2/-1}$ disconnections.

Figure 9. Dichromatic patterns showing the relevant translation vectors and step heights for (a) a $\mathbf{b}_{1/0}$ dislocation and (b) the $\mathbf{b}_{3/1}$ and $\mathbf{b}_{-2/-1}$ disconnections.

Figure 10. An instantaneous simulation of a $\mathbf{b}_{3/1}$ disconnection moving in response to an applied shear strain.

Figure 11. Contour plot of the γ-surface for the coherent interface; the origin represents the observed configuration which is the only stable form.

Figure B 1. Schematic illustration of the overlap step and dislocation contributions to the atomic flux accompanying lateral motion of a disconnection. The flux due to motion of the step portion, N_s, is associated with *transfer* of material from one crystal to the other, whereas that due to motion of the dislocation portion, N_d, involves matter flow only in the upper crystal in this case. (For simplicity, the disconnection is depicted before the Volterra operation to close the gap has been carried out.) These two fluxes are quantified by the two terms in expression (A 1).

Figure C 1. Schematic illustration showing the disconnection and 'coherency-producing' defect content of an interface, with Burgers vector components resolved in the coherent interface (upper) and habit plane (lower) frames. The terrace plane is

inclined at an angle θ to the horizontal habit plane, and the disconnections are separated by the distance $d = \lambda_D$.

TABLES

Table 1: Crystallographic Parameters for the interfacial defects analyzed in this study. The quantities are expressed in the λ coordinate frame in units of the lattice parameter, a.

Defect	**t**(λ)	**t**(μ)	**b**	magnitude	b_n	b_e
$\mathbf{b}_{-5/-2}$	$\frac{1}{2}[\bar{2}1\bar{1}]$	$\frac{1}{2}[112]$	[-0.390, -0.554, -0.390]	0.781	0.134	0.770
$\mathbf{b}_{3/1}$	$\frac{1}{2}[0\bar{1}1]$	$\frac{1}{2}[\bar{1}\,\bar{1}0]$	[-0.097, -0.140, -0.097]	0.196	0.035	0.192
$\mathbf{b}_{-8/-3}$	$[\bar{1}1\bar{1}]$	$[111]$	[-0.293, -0.414, -0.293]	0.586	0.099	0.577
$\mathbf{b}_{1/0}$	$\frac{1}{2}[\bar{1}\,\bar{1}0]$	0	$\frac{1}{2}[\bar{1}\,\bar{1}0]$	0.707	0.204	0.577
$\mathbf{b}_{3/1}$	$\frac{1}{2}[0\bar{1}1]$	$\frac{1}{2}[\bar{1}\,\bar{1}0]$	[-0.097, -0.140, -0.097]	0.196	0.035	0.192
$\mathbf{b}_{-2/-1}$	$\frac{1}{2}[\bar{1}0\bar{1}]$	$\frac{1}{2}[110]$	[-0.403, -0.360, -0.097]	0.549	0.169	0.384

Table 2**:** Summary of Circuit Analyses for Interfacial Disconnections and Dislocation. $\mathbf{C}_\lambda$ and $\mathbf{C}_\mu$ are expressed in the λ and μ coordinate frames respectively. $\mathbf{b} = -(\mathbf{C}_\lambda + \mathbf{P}_c\mathbf{C}_\mu)$ is expressed in the λ coordinate frame.

$\mathbf{b}_{\lambda/\mu}$	$\mathbf{C}_\lambda$	$\mathbf{C}_\mu$	**b**	h(λ)	h(μ)

$b_{-5/-2}$ (figure 4)	ABCDE: $\frac{1}{4}[27\ 22\ 27] \pm \frac{1}{4}[\bar{1}01]$	FGHI: $\frac{1}{4}[-15\ \ 38\ \ -15] \pm \frac{1}{4}[\bar{1}01]$	[-0.390, -0.554, -0.390]	$-\frac{5}{2\sqrt{6}} = -5d_{242}$	$-\frac{2}{\sqrt{3}} = -2d_{111}$
$b_{-5/-2}$ (figure 5)	ABCDE: $\frac{1}{4}[35\ \ 30\ \ 35] \pm \frac{1}{4}[\bar{1}01]$	FGHI: $\frac{1}{4}[-21\ \ 50\ \ -21] \pm \frac{1}{4}[\bar{1}01]$	[-0.390, -0.554, -0.390]	$-\frac{5}{2\sqrt{6}} = -5d_{242}$	$-\frac{2}{\sqrt{3}} = -2d_{111}$
$b_{3/1}$	E'D'DE: $\frac{1}{4}[15\ \ 18\ \ 15] \pm \frac{1}{4}[\bar{1}01]$	FGG'F': $\frac{1}{4}[-13\ \ 22\ \ -13] \pm \frac{1}{4}[\bar{1}01]$	[-0.097, -0.140, -0.097]	$\frac{3}{2\sqrt{6}} = 3d_{242}$	$\frac{1}{\sqrt{3}} = d_{111}$
$b_{-8/-3}$	ABCD'E': [535]	F'G'HI: $[\bar{2}7\bar{2}]$	[-0.293, -0.414,-0.293]	$-\frac{4}{\sqrt{6}} = -8d_{242}$	$-\frac{3}{\sqrt{3}} = -3d_{111}$
$b_{1/0}$ (figure 7)	ABCDE: $\frac{1}{4}[17,18,17] \pm \frac{1}{4}[\bar{1}01]$	FGHI: $3[\bar{1}2\bar{1}]$	$\frac{1}{2}[\bar{1}\ \bar{1}\ 0]$ or $\frac{1}{2}[0\ \bar{1}\ \bar{1}]$	$\frac{1}{2\sqrt{6}} = d_{242}$	0
$b_{1/0}$ (figure 8)	ABCDE: $\frac{1}{4}[33\ \ 34\ \ 33] \pm \frac{1}{4}[\bar{1}01]$	FGHI: $6[\bar{1}2\bar{1}]$	$\frac{1}{2}[\bar{1}\ \bar{1}\ 0]$ or $\frac{1}{2}[0\ \bar{1}\ \bar{1}]$	$\frac{1}{2\sqrt{6}} = d_{242}$	0
$b_{3/1}$	E'D'DE: $\frac{1}{4}[15,18,15] \pm \frac{1}{4}[\bar{1}01]$	FGG'F: $\frac{1}{4}[-13,22,-13] \pm \frac{1}{4}[\bar{1}01]$	[-0.097, -0.140, -0.097]	$\frac{3}{2\sqrt{6}} = 3d_{242}$	$\frac{1}{\sqrt{3}} = d_{111}$
$b_{-2/-1}$	ABCD'E': $\frac{1}{2}[989]$	F'G'HI: $\frac{1}{4}[-11,26,-11] \pm \frac{1}{4}[\bar{1}01]$	[-0.403, -0.360, 0.097] or [0.097, -0.360, -	$-\frac{1}{\sqrt{6}} = -2d_{242}$	$-\frac{1}{\sqrt{3}} = -d_{111}$

			0.403]		

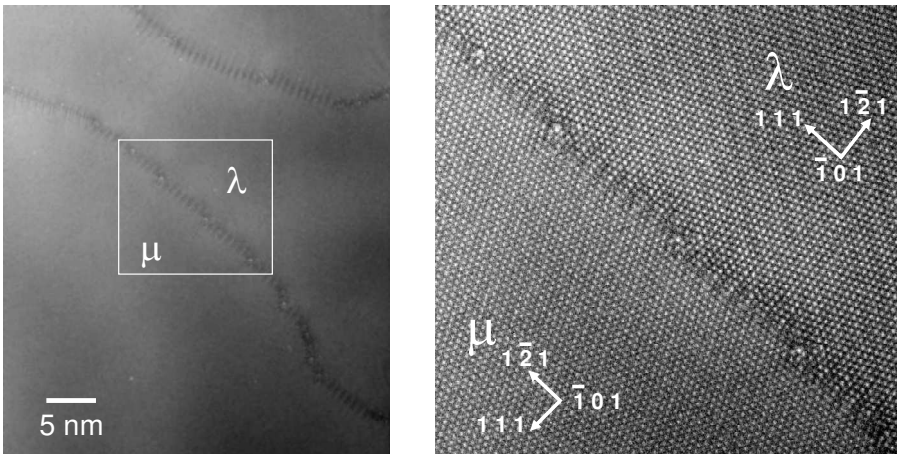

Figure 1.

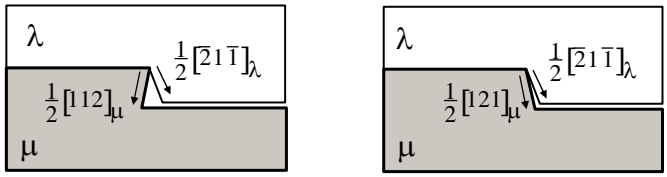

Figure 2.

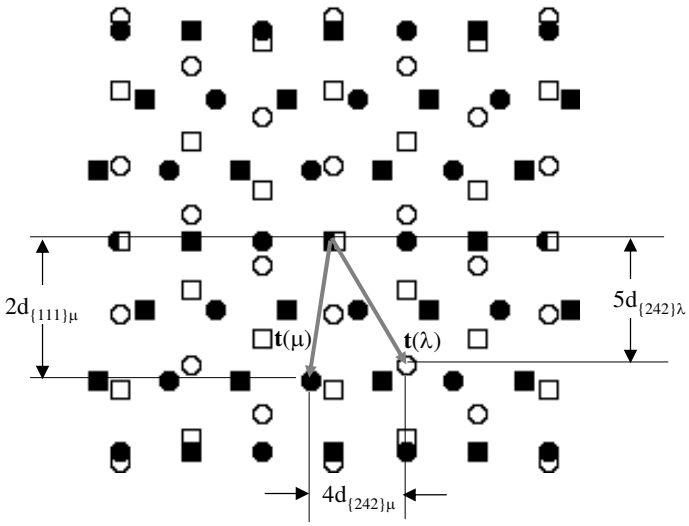

Figure 3.

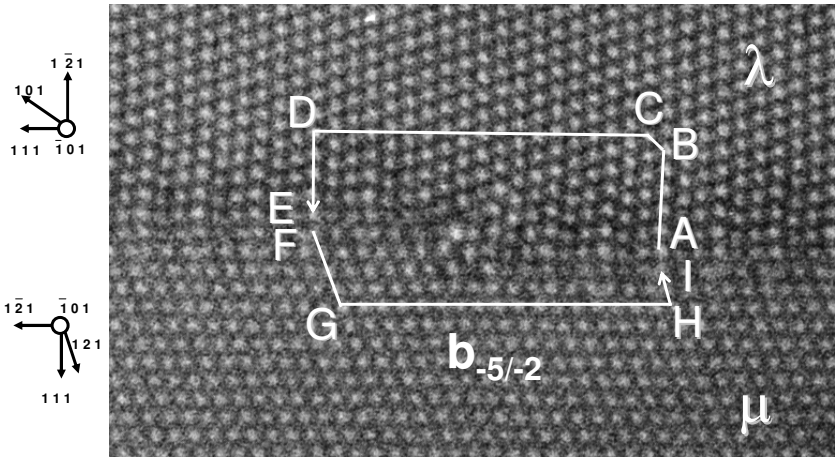

Figure 4.

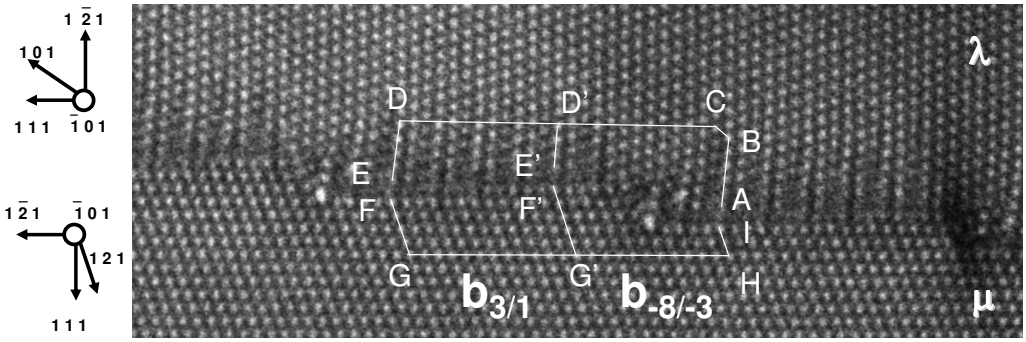

Figure 5.

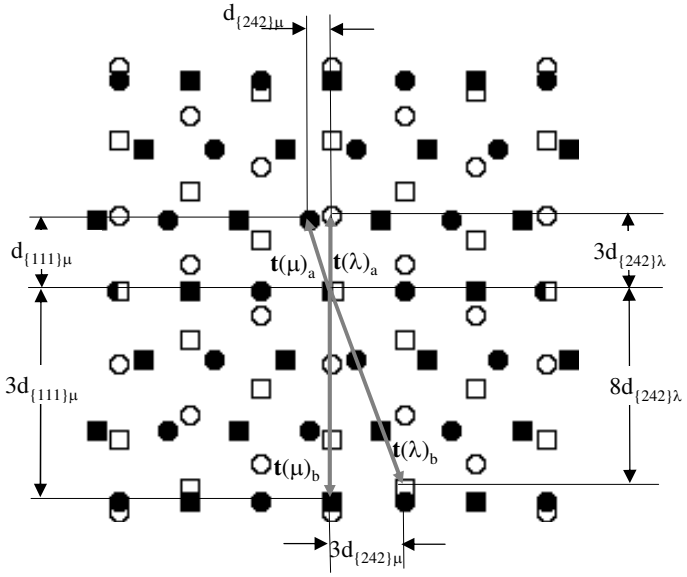

Figure 6.

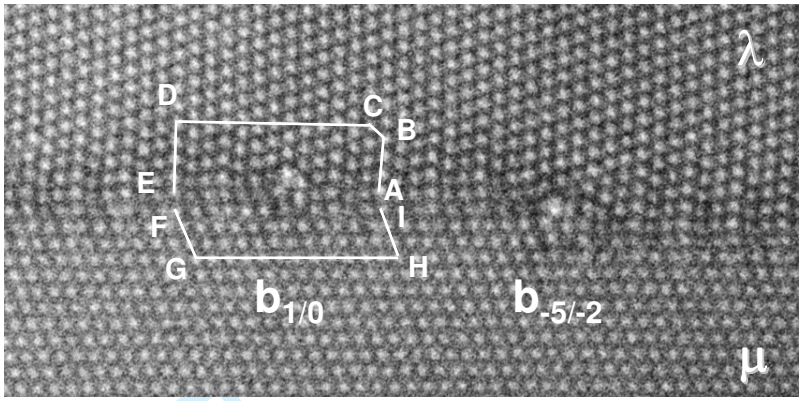

Figure 7.

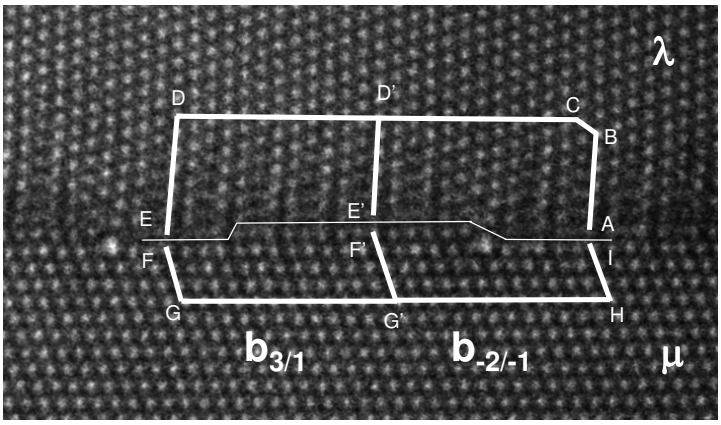

Figure 8.

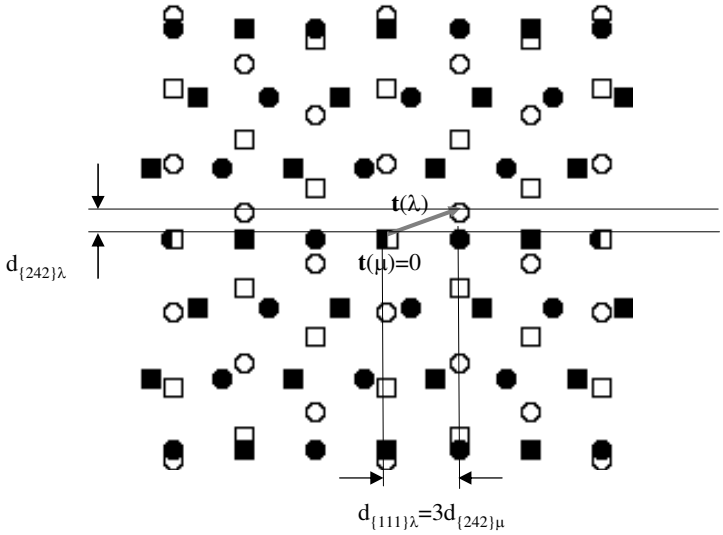

Figure 9(a)

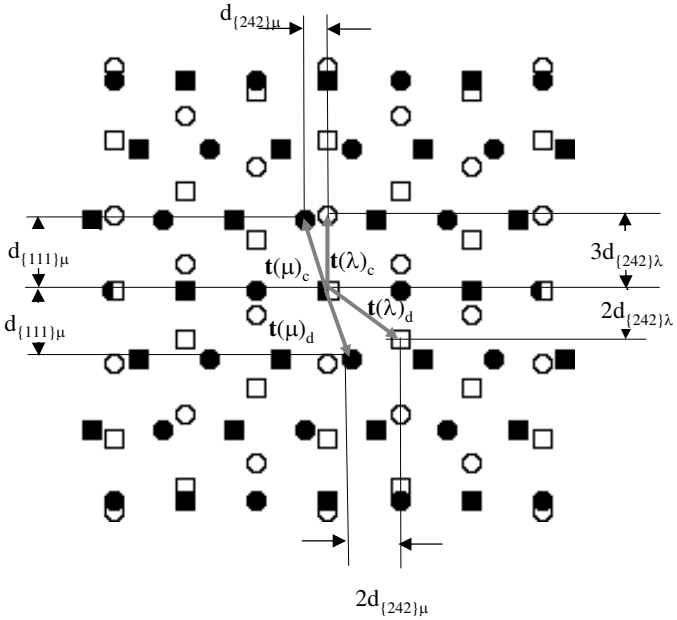

Figure 9(b)

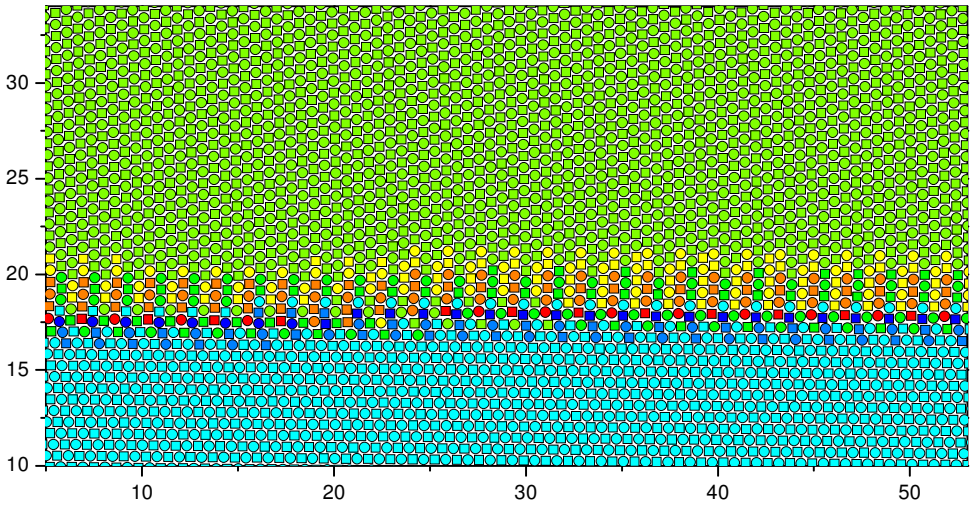

Initially the boundary was at z=21

Figure 10

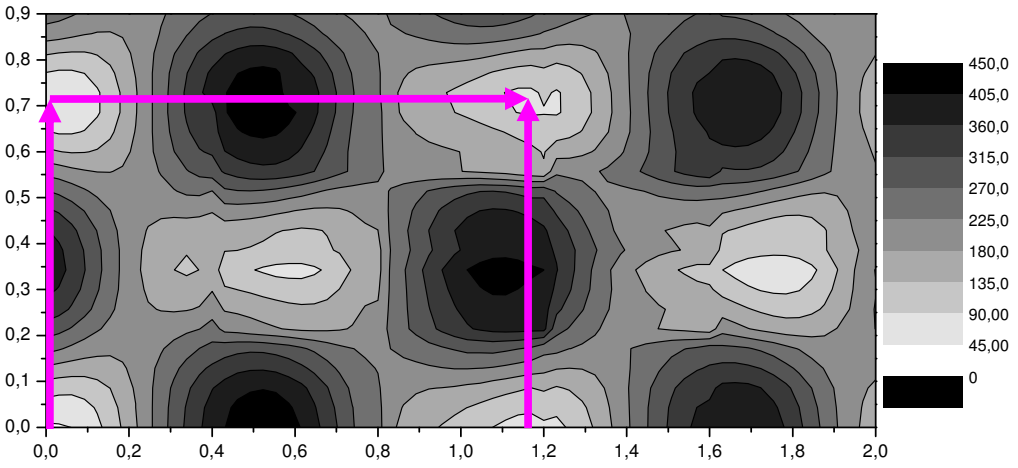

Surface energy is in mJ/m^2 and distances are in lattice parameters

Figure 11.

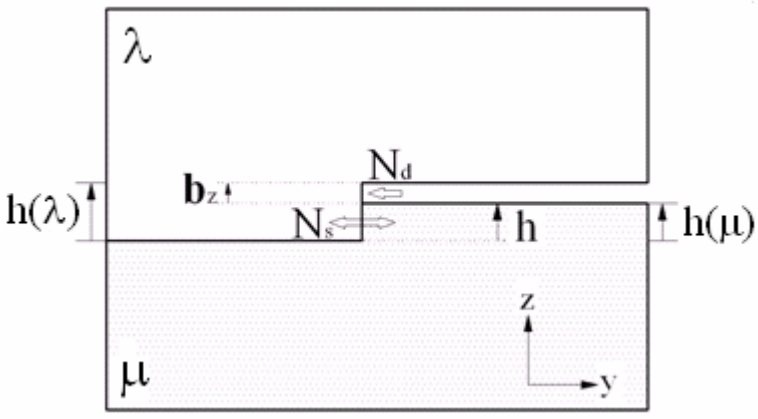

Figure B 1

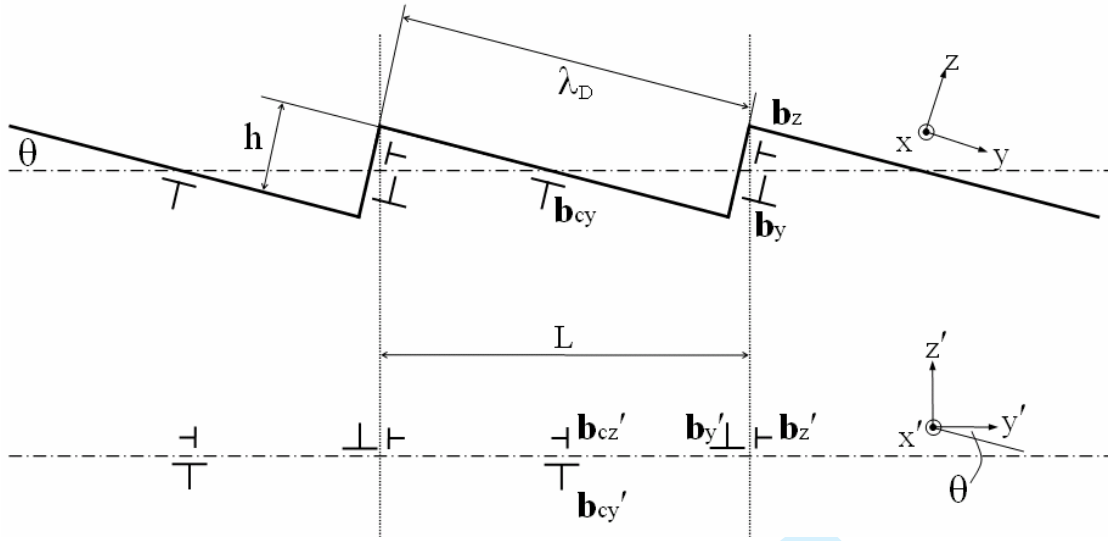

Figure C 1